

The effect of cube-roughened walls on the response of rough-to-smooth (RTS) turbulent channel flows

Umair Ismail^{*,a}, Tamer A. Zaki^b, Paul A. Durbin^a

^a Department of Aerospace Engineering, Iowa State University, Ames, IA 50011, USA

^b Department of Mechanical Engineering, Johns Hopkins University, Baltimore, MD 21218, USA

ABSTRACT

Direct numerical simulations of cube-roughened rough-to-smooth channel flows are performed with the objective of studying the response of turbulence statistics in the developing flow over smooth walls. Non-equilibrium effects persist and the global recovery is slow and incomplete by the streamwise exit of the computational domains, which is at about 10 channel half heights. The estimated recovery distance in the outer regions of the flow is on the order of 50 channel half heights, but different statistics have disparate relaxation rates. The turbulence structure swiftly relaxes to a ‘near’ equilibrium very close to the wall. Within this wall layer, due to a strong mean shear, turbulence statistics and instantaneous motions resemble their fully-smooth equivalents. However, the reversion is not complete because it is interrupted by large structures that persist from the upstream roughness. As the flow encounters the step change in roughness, it expands producing strong mean-advection effects, which prevent the canonical log-law region from being established. The expansion of the mean flow also results in an adverse pressure gradient across the channel. It recovers gradually, only becoming favourable near the exit of the computational domains.

1. Introduction

Extensive experimental and computational studies of fully developed, smooth- and rough-wall turbulent flows have led to a detailed picture of the dynamics of turbulence in these configurations. However, the non-equilibrium, intermediate regimes where the flow undergoes rough-to-smooth or smooth-to-rough transition are less clear. In addition to providing estimates for the distances required to achieve one fully developed state when starting from the other, experiments with these configurations can also highlight near-wall effects that are otherwise concealed in statistically stationary flows.

The chief difference between fully developed rough- and smooth-wall flows is in their turbulence structures. For the smooth case, the region very close to the wall is occupied by the viscous and buffer layers, that form part of a larger self-sustaining ‘cycle’. Within the buffer layer, the predominant momentum balance is between the viscous and the Reynolds-stress gradients, while the pressure term is negligible. Above fully-rough walls, a roughness sublayer exists in which spatial inhomogeneity persists despite time averaging (Raupach et al., 1991). The term fully-rough refers to configurations where k_s is larger than about 90 viscous units (Durbin and Reif, 2011), where k_s is the effective sand-grain lengthscale – a roughness parameter

obtained when the results from a particular rough-wall experiment are equated with the lab experiments by Nikuradse (1933). The frictional drag of fully-rough walls is independent of the kinematic viscosity, ν , and only a function of the roughness type and size. Part of this roughness sublayer, unlike fully-smooth walls, shows a momentum balance among all four terms, including the advection term (Ikeda and Durbin, 2002). Additionally, rough walls serve the purpose of shifting the turbulence structure away from it. In the context of channels flows with asymmetric roughness, this leads to mean-velocity profiles with their peaks located closer to the smooth wall.

This study is an extension of the preliminary results presented at the Tenth International Turbulence Shear Flow Phenomena conference (see Ismail et al., 2017). It examines rough-to-smooth (RTS) transition in cube-roughened channel flows. This configuration is a subset of the larger class of non-equilibrium flows between two statistically stationary states. Previous studies include the lab experiments by Antonia and Luxton (1972) and Hanson and Ganapathisubramani (2016), which are perhaps the most comprehensive. These experiments show that the turbulence statistics near the wall recover quickly in comparison to the outer flow, but the overall recovery progresses slowly. Furthermore, the uncertainties involved in measuring the skin friction and other flow statistics both at the rough

* Corresponding author.

E-mail addresses: umair@iastate.edu (U. Ismail), t.zaki@jhu.edu (T.A. Zaki), durbin@iastate.edu (P.A. Durbin).

wall and immediately after the change in roughness complicate the ability to draw conclusions. These difficulties motivate performing resolved computer simulations that can accurately measure the skin friction, and enable identification of dynamical effects near the wall that are difficult to probe experimentally. It is worth emphasizing that after a sudden change in roughness, channel flows respond differently from experimental predictions for boundary layers, particularly away from the wall. This is evidenced by our earlier work on rib-roughened, RTS channel flow (Ismail et al., 2018), and is also clear from the results discussed herein.

2. Numerical approach

The incompressible Navier–Stokes equations are solved using the iterative, semi-implicit, fractional time-step method by Pierce and Moin (2004), which is second-order accurate in both space and time. The time discretization is similar to the Crank–Nicolson time-advancement scheme. Both the viscous and advection terms in the wall-normal direction are treated implicitly. The three-dimensional, finite-differenced, pressure Poisson equation for simulations with cube-roughened walls is solved using an iterative, preconditioned multigrid linear solver from the Hypre library (Falgout and Yang, 2002). For cases with rib-roughened and smooth walls, to improve computational efficiency, Fourier decomposition is used in the spanwise direction, and the resulting two-dimensional Helmholtz equation is solved using a linear solver from the Hypre library. Roughness is modelled using an ‘blanking’ approach, where the non-fluid grid points are effectively decoupled from the fluid points before solving a system of linear equations. Validation was performed against the direct numerical simulation (DNS) studies by Moser et al. (1999), Leonardi et al. (2003) and Orlandi et al. (2006) in order to establish the accuracy of our DNS. Some of these smooth-wall and rough-wall simulations are discussed by Ismail et al. (2018).

3. Computational setup

The simulations are divided into two parts: an initial, auxiliary computation is used to simulate the flow over the rough wall and to generate inflow conditions for the main, downstream simulation. The later is meant to calculate the developing flow within a channel. The connection between the two parts is shown schematically in Fig. 1. The upper walls in both the auxiliary and main components are kept smooth.

The streamwise extent of the rough-wall section is denoted by L_{rs} . The inflow condition to that section is provided by recycling; a cross-flow plane of the instantaneous velocity field, u_i , located at L_{fd} downstream of the inflow is extracted and then applied at the inflow. Here, $i = 1, 2, 3$ indicate the streamwise (x), wall-normal (y) and spanwise (z) directions, respectively. In this study, overline and prime, e.g. $\bar{\alpha}$ and α' , indicate the mean and fluctuating components of an instantaneous field α .

Results from two types of rough surfaces, cube- and rib-roughened walls, are discussed. For the former, a staggered arrangement of the roughness elements is employed and each surface is parametrized using A_c/A_t , where A_t is the total area of the wall covered by one repeating unit and A_c is the area occupied by a cube within a repeating unit. An example with four repeating units highlighted is shown schematically in Fig. 2a.

The start of the transitional regime, at $x/\delta = 0$, is identified as the point where the last roughness repeating unit ends. Since we document results for three different developing smooth walls, six simulations in total were performed. Three of these are for the initial rough walls, and the other three compute the downstream flow developing over smooth walls. The bulk Reynolds number is maintained at $Re_b = U_b \delta / \nu = 18,000$. Here, U_b and δ are the bulk velocity and the channel half height. This Re_b is equivalent to a fully developed, smooth-wall channel flow with

an approximate friction Reynolds number, $Re_\tau = 920$. The roughness height for both the cube- and rib-roughened cases is fixed at $\delta/k = 12$. Details of the flow configurations, e.g. the domain sizes (L_x, L_y, L_z), are listed in Table 1. In the table and throughout this work, the numeral in the labels for different cases is used to denote whether the simulation is of the fully developed rough wall or of the developing smooth wall. For example, the fully developed rough wall portion of case A is labelled A1 and the developing smooth wall component as A2. To generate inflow conditions for the cases labelled X2, instantaneous cross-flow planes from the fully developed, rough wall simulations are extracted and stored. These planes are located at a distance L_{ip} downstream of $x = 0$.

The only rib-roughened simulation (case C) in the present study is the same as case B by Ismail et al. (2018). Except, over there, both the initial rough wall and the downstream developing smooth wall components were simulated together. For this case, the spacing between successive roughness elements is $w = 9k$ (see the schematic in Fig. 2b). This spacing is wide enough to ensure k -type roughness behaviour (Leonardi et al., 2003; Ikeda and Durbin, 2007). Unlike the cube-roughened cases, the inflow generation plane for case C is located in the rough-wall section, at $x/\delta = -1.67$, which coincides with the recycling station. Fig. 4, presented in a later section, compares the skin friction over the developing, smooth wall from case C2 and case B by Ismail et al. (2018), and a favourable agreement is observed. Furthermore, above the rough wall, the skin friction between the two only differs by about 1%. This ensures that the turbulence statistics are nicely reproduced when inflow boundary conditions generated from a separate simulation are used to compute the developing flow over the smooth wall.

Uniform grid spacing is used in the streamwise and spanwise directions, with grid stretching in the wall-normal direction. About 75 grid points are packed below $y/\delta = 0.1$ for all cases. The grid resolution is reported in Table 2, and is comparable to that used by Leonardi and Castro (2010), Ikeda and Durbin (2007) and Ismail et al. (2018). No-slip boundary conditions are applied at all solid surfaces, and a convective boundary condition of the form $\partial u_i / \partial t + c \partial u_i / \partial x = 0$ is applied at the outflow, where c is the local bulk velocity.

4. Flow over the rough wall

In this section, we characterize the initial rough-wall regime. Some relevant parameters are listed in Table 3. The friction Reynolds number on the rough wall is defined as $Re_{\tau R} = u_{\tau R} \delta / \nu$, where $u_{\tau R}$ is the friction velocity and is calculated using both the viscous and pressure drags, D_v and D_p , on the lower wall. The viscous term D_v involves viscous contributions from horizontal no-slip surfaces at $y = 0$ and $y = k$, and from vertical, $x - y$, no-slip planes of the roughness elements. Inner-scaled mean-velocity profiles, \bar{U}_R^+ , for the three different cases are shown in Fig. 3a. Also plotted are rough wall logarithmic fits of the form

$$\bar{U}^+ = (1/0.41) \log(y_m^+) + A,$$

where $y_m = y - d$ and A is the wall intercept. Using d in the definition of y_m is akin to shifting the lower wall upwards. The utility of fitting the logarithmic law to the mean velocity is simply to equate the present results with those by Nikuradse (1933), and then estimate an equivalent sand-grain roughness size, k_s^+ . The expected increase in k_s^+ with increasing $Re_{\tau R}$ is evident from Table 3. The value of d , which is typically between $0 < d < k$, is determined by optimizing a logarithmic fit to the averaged mean-velocity profiles; it is $d = 0.6k$ and $d = 0.5k$ for case A and B, respectively. This compares favourably with the range reported by Leonardi and Castro (2010), which is about $d/k = 0.4 - 0.6$ at similar A_c/A_t . Squire et al. (2016) adopted a value of $d = 0.5k$ in their boundary-layer experiments, but they did not resolve the roughness canopy. It is worth emphasizing that using a non-zero d , while keeping κ fixed within its commonly accepted range of $0.40 - 0.42$, is essential in order to produce an acceptable log-law fit. Using $d = 0$ would result in a

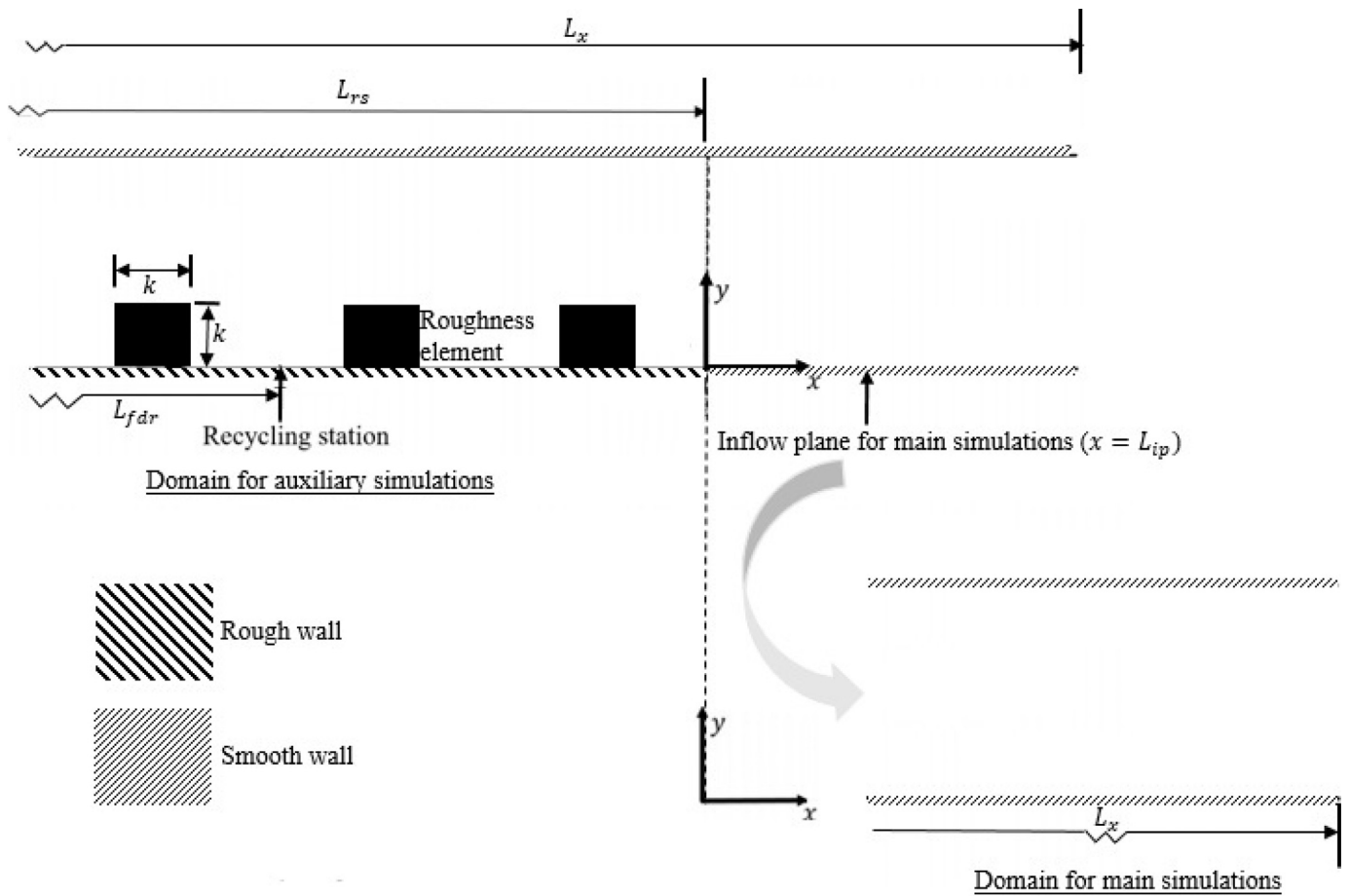


Fig. 1. Schematic of side view (xy-plane) of the computational domain. This schematic is not drawn to scale.

κ that varies with the present roughness morphology, A_c/A_t . In fact, some literature on atmospheric boundary layers indeed argues in the favor of a non-universal κ (see Frenzen and Vogel, 1995). Alternatively, calculating d independently, e.g. using the approach by Jackson (1981), still produces a von-Karman constant that depends on the roughness. This methodology was one of the two approaches used by Leonardi and Castro (2010) to optimize their logarithmic fits. We have used $d = 0$ for the rib-roughened surface, case C. As done by Ismail et al. (2018) and Ikeda and Durbin (2007), an acceptable log-law profile was successfully identified without displacing the rib-roughened wall. The observation that the fitted logarithmic profile extends down into the region with

spatial mean flow inhomogeneity suggests the existence of an overlap between the roughness sublayer (RS) and the log-law region. Here, the notion of a RS is used to identify the region above the rough wall where horizontal inhomogeneity in the mean velocity persists. For cube-roughened walls, case A and B, the RS extends up till $2k - 2.5k$. This is smaller than the extent of the RS for rib-roughened walls, case C here and other simulations by Ismail et al. (2018), which is about $4.5k$. Leonardi and Castro (2010) identified this height at $y = 1.5k$ from the approximate convergence of turbulence stress profiles in their cube-roughened, half-channel simulations. Like the values for d , a good agreement with the results by Leonardi and Castro (2010) is also

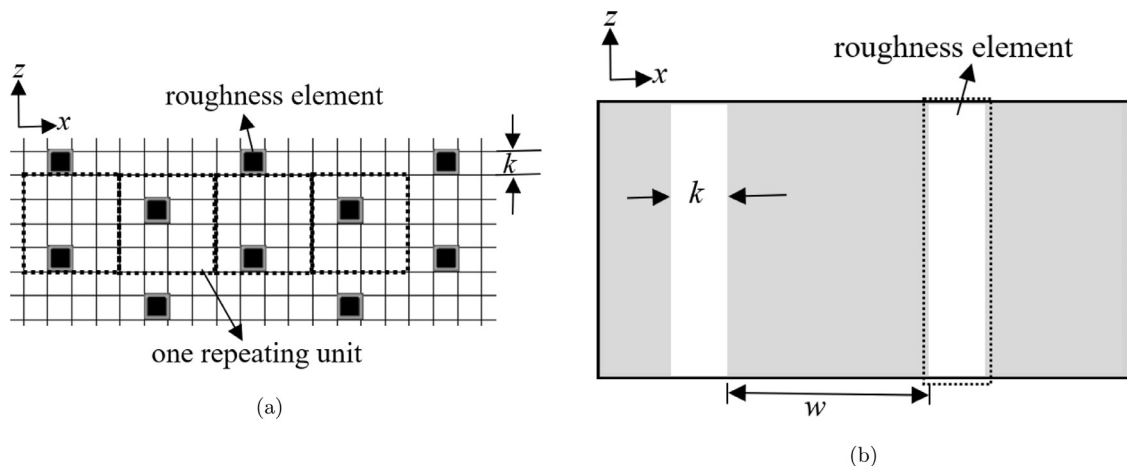


Fig. 2. Schematics of top views (xz-plane) of the rough wall setups (a) for case B with $A_c/A_t = 1/16$ and (b) for case C with $w/k = 9$. These schematics are not to scale.

Table 1
Summary of few of the computational parameters from different simulations. RU: repeating unit.

Case	Number of grid points	$(L_x \times L_y \times L_z)/\delta$	L_{rz}/δ	L_{fdr}/δ	w/k	A_c/A_t	RUs in x	RUs in z	L_{ip}/δ
A1	1200 × 376 × 288	8.33 × 2.00 × 2.00	7.00	6.00	–	1/9	28	8	0.25
B1	1300 × 376 × 240	10.83 × 2.00 × 2.00	7.33	6.00	–	1/16	22	6	0.33
C1	1200 × 379 × 288	8.33 × 2.00 × 2.08	7.50	5.83	9	–	9	–	–1.67
A2	1200 × 376 × 288	8.33 × 2.00 × 2.00	–	–	–	–	–	–	–
B2	1300 × 376 × 240	10.83 × 2.00 × 2.00	–	–	–	–	–	–	–
C2	1200 × 379 × 288	8.33 × 2.00 × 2.08	1.67	–	9	–	2	–	–

Table 2
Spatial resolutions for the different cases. The normalization is with the friction velocity at the upper smooth wall in the fully developed rough-wall region, $u_{\tau,s}$.

Case	Δx_s^+	Δz_s^+	$\Delta y_s^+ _{min}$	$\Delta y_s^+ _{max}$
A	7.08	7.08	0.400	7.00
B	9.00	9.00	0.399	6.99
C	7.73	8.05	0.436	7.65

Table 3
Parameters categorizing the different rough wall setups. $Re_{\tau,RU}$ is the frictional-Reynolds-number at the upper wall.

Case	$Re_{\tau,R}$	$Re_{\tau,RU}$	A	k_p/k	k_s^+	D_v/D_p (in %)
A1	1602	1019	–5.7	2.53	338	7.8
B1	1519	1013	–4.8	1.84	233	18.4
C1	2220	1115	–9.5	8.49	1570	3.8

obtained for D_v/D_p . These ratios for different cases are reported in Table 3.

Fig. 3b shows the wall-normal variation of the mean momentum balance in the fully developed rough regime for case A1. Within the roughness canopy, all four terms are active. The Reynolds stress term, $\partial(-\overline{u'_i u'_j})/\partial x_j$, shows a positive contribution to the mean-momentum balance from the rough wall up till approximately $y \approx 1.2k$. Since this Reynolds-stress term is essentially $\partial(-\overline{u'v'})/\partial y$, this translates to vertical fluxes of $\overline{u'v'}$ towards the wall. Slightly above this height, at $y/\delta = 1.6$, the viscous term becomes negligible and the situation reverts to the balance characteristic of fully developed smooth-wall flow, between the pressure and Reynolds stress gradient, only.

5. Developing flow over the smooth wall

The flow in the developing, smooth-wall regime (simulations A2, B2 and C2 from Table 1) is discussed in this section. The skin friction is reported first, followed by mean-flow and turbulence statistics. Finally, instantaneous fields are shown to provide an empirical view of the

changes in the turbulence.

5.1. Skin friction

The streamwise variation of skin friction for different cases is plotted in Fig. 4a–c. These profiles are calculated simply as $C_f = (1/U_c)^2(\nu \partial \overline{U}/\partial y)$ at the horizontal, no-slip surfaces. Here, $U_c = 1.5U_b$ is the laminar centerline velocity. Additionally, the constant, total skin friction levels in the fully developed rough-wall regime (labelled FDR) are also shown, and include both the viscous and form drags, as noted in the previous section. Fig. 4a includes an additional developing smooth-wall case labelled A22. Unlike A2, the inflow plane for this case is extracted from between two roughness repeating units, at $x/\delta = -1$. The results demonstrate that the location of the inflow plane does not alter the development of C_f , as the profiles for both cases A2 and A22 are identical for $x/\delta > 0.25$. To simplify identifying different profiles in Fig. 4, the C_f variation in Fig. 4b at the lower wall, upper wall and in the fully developed regime are labelled individually using curly braces.

On entering the transitional regime, at $x/\delta = 0$, the skin friction first decreases sharply to levels below those shown by fully developed smooth walls. For cube-roughened walls, the minimas in the transitional regime stay positive. Separation bubbles behind these cubes only occupy a small fraction of the entire spanwise width of the computational domains. This is not true for the rib-roughened case where, due to a separation bubble downstream of the last roughness element, the C_f is forced below zero.

After that adjustment, the skin friction shows a sharp initial increase and then virtually levels off by $x/\delta \approx 2 - 3$. Despite this plateau, the skin friction has not recovered to fully developed, smooth-wall levels. Recovery is incomplete by the end of the computational domains. This behaviour is more evident for the cube-roughened cases (Fig. 4a and b). For case B which has a lower k_s^+ , a sharper increase is observed after the initial decrease in the transitional regime. This is consistent with the observation made from case A and case B by Ismail et al. (2018) and from the results by Antonia and Luxton (1972); however, it should be emphasized that simulations by Ismail et al. (2018) had different bulk

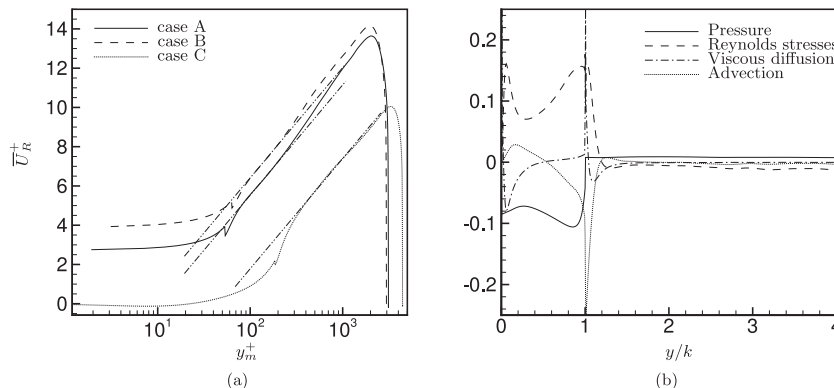


Fig. 3. (a) Inner-scaled mean streamwise velocity, \overline{U}_R^+ , in the fully developed rough-wall regime. (b) Mean-momentum budget in the fully developed rough-wall regime for case A. All the terms are on the right hand side of the mean momentum equation and have been normalized by U_b^2/δ .

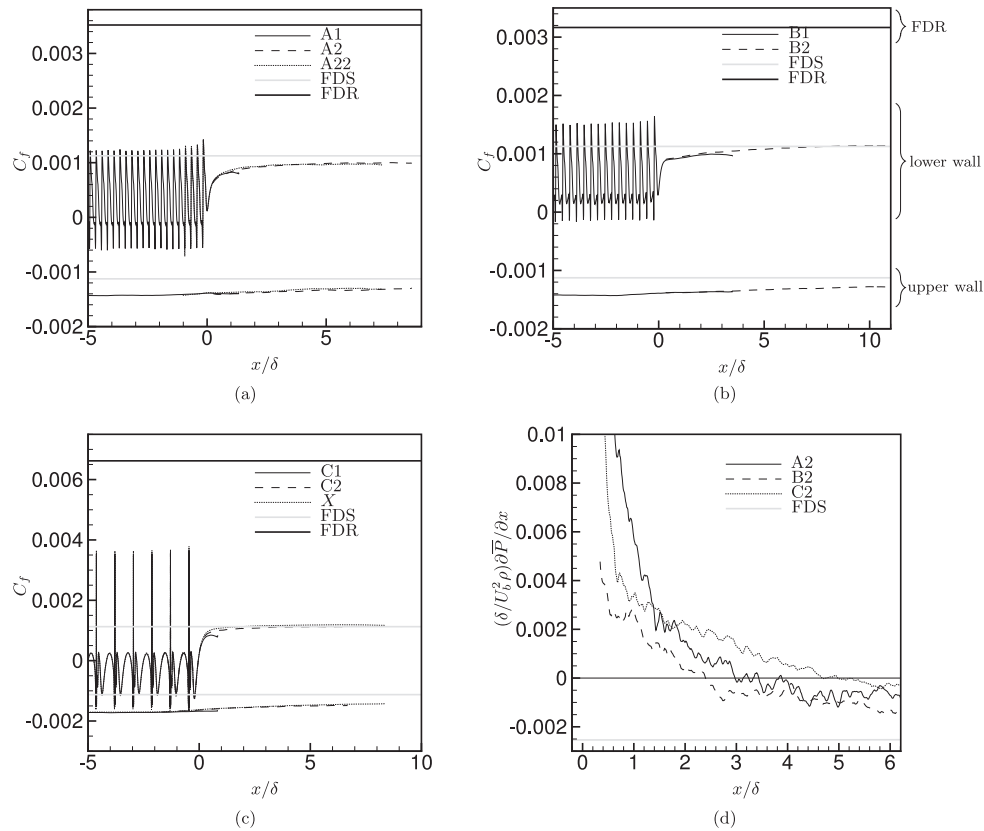


Fig. 4. C_f variation with the streamwise distance for cases labelled (a) A, (b) B and (c) C. For $x/\delta > 0$, the profiles above $C_f = 0$ are over the developing smooth wall at $y = 0$ and the profiles below $C_f = 0$ are at the developing upper wall at $y = 2\delta$. The profile labelled X in (c) is case B from Ismail et al. (2018). FDR: Fully developed rough wall, FDS: Fully developed smooth wall. (d) Streamwise variation of $(1/\rho)\partial\bar{P}/\partial x$ over the lower, developing smooth wall.

Reynolds numbers and the same δ/k ratios.

Further details of this incomplete recovery of C_f are provided by evaluating $(1/\rho)\partial\bar{P}/\partial x$ at the lower wall, where \bar{P} is the mean pressure (Fig. 4d). As a consequence of the mean momentum equation, $(1/\rho)\partial\bar{P}/\partial x = \nu\partial^2\bar{U}/\partial y^2$ at the wall. The adverse pressure gradient at the rough wall continues to persist downstream, only becoming favourable by the streamwise end of the computational domain. As will be seen later, the behaviour of the skin friction is paralleled by a slow and incomplete recovery of the mean velocity field.

The recovery at the upper wall is no different. However, there the skin friction does not plateau; instead it decays steadily. Exponential fit of the form $C_f \sim (x/\delta)^{-0.008}$ reveals that, for case A, a streamwise fetch length of about 26δ might be needed for the skin friction at the upper wall to attain fully developed levels.

The skin friction can be interpreted as the force input by the wall into the flow, which is required to accelerate the mean profile, overcome the dissipation in the mean and to produce the turbulence kinetic energy (Renard and Deck, 2016). The slow recovery of the skin friction is thus tied to a gradual change in the mean-flow profile and the turbulence stresses as they relax towards the smooth-wall values.

5.2. Mean velocity

The downstream variation of the mean streamwise velocity, \bar{U}/U_b , is reported in Fig. 5a–c. The fully developed profiles in Fig. 5a are labelled explicitly to improve readability of the mean-velocity profiles at different streamwise stations. Above the rough wall, both horizontal and time averaging are employed, while in the non-equilibrium region the profiles are only averaged in time and the spanwise direction. In the fully developed rough-wall regime, the influence of k_s^+ is evident below $y = k$. Among the three cases studied, the rib-roughened wall shows the

smallest slope of \bar{U} near the lower wall. This is due to its large blockage effect and hence a large form drag. At the upper smooth wall, the profile appears fuller for case C, that is the one with a higher $Re_{e, RU}$. This is consistent with the appearance of fully developed smooth-wall profiles at different Re_e (see Moser et al., 1999). In the developing regime, the mean velocity accelerates near the lower wall with streamwise distance, and decelerates in the outer flow. The acceleration and deceleration are a mere consequence of continuity. Again, the effect of different rough surfaces on the streamwise relaxation in the different cases is evident. The relaxation of mean velocity in the outer flow between different cases can be compared by tracking the peak of \bar{U} with x/δ (Fig. 5d). Clearly, the peaks for the cube-roughened cases decay at a slower rate. It should, however, be emphasized that peak for the rib-roughened surface lies further away from the lower wall. It has to, therefore, decrease more in magnitude when approaching the smooth-wall level. This relatively quick decay for the rib-roughened walls is attributed to their stronger advective and turbulence-stress fluxes over the entire wall-normal range. Supporting evidence is provided by the mean-momentum budgets at two streamwise stations (Fig. 6). With downstream distance, the momentum fluxes diminish but the influence of the roughness continues. When the mean flow expands after the step-change in roughness, it creates an adverse pressure gradient across the whole channel; however, unlike fully developed smooth-wall flows, this pressure gradient is a small component among all the momentum-balance terms.

It could be instructive to use the wall-normal variation of different terms in the mean-momentum balance to classify the developing flow over smooth walls. Very close to the wall, at $x/\delta = 4$ in Fig. 6c, there is a qualitative resemblance among the terms of different RTS cases and the fully developed smooth-wall channel. The resemblance is in profile shapes and virtually identical locations of the respective peaks.

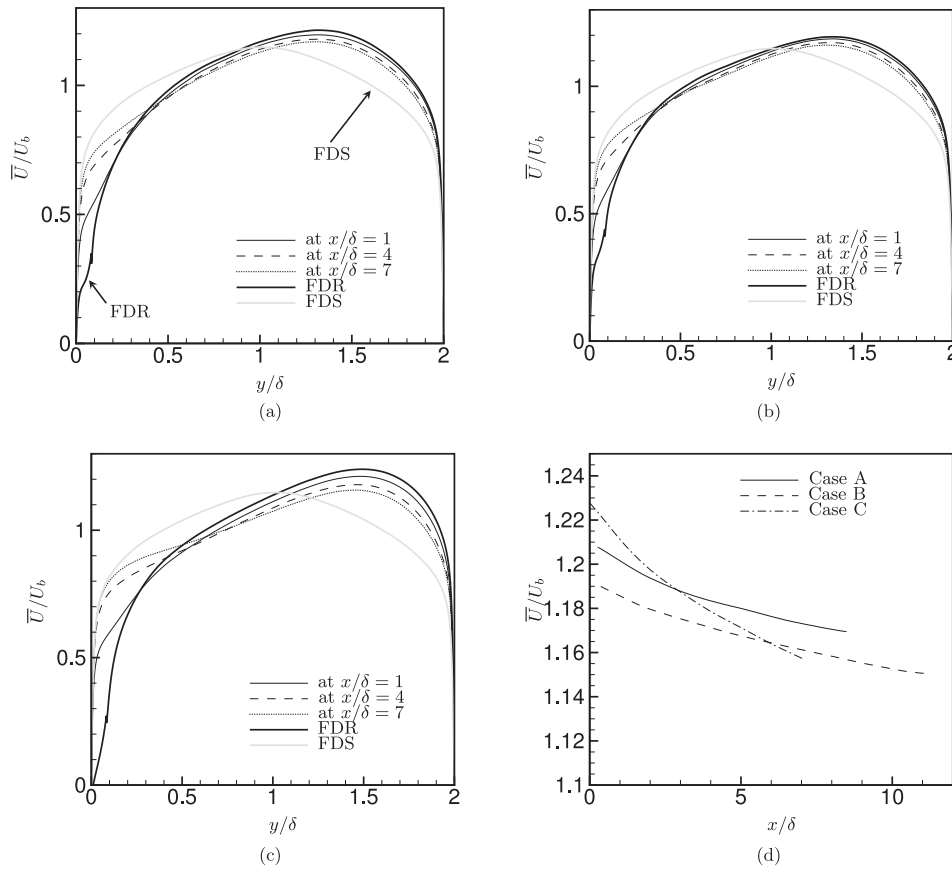


Fig. 5. \bar{U}/U_b variation with the streamwise distance for cases labelled (a) A, (b) B and (c) C. FDR: Fully developed rough wall, FDS: Fully developed smooth wall. (d) Streamwise variation of the peaks of \bar{U} for different cases.

Nonetheless, the influence of upstream roughness lengthscales is not absent entirely, as the peak magnitudes differs across the three RTS cases. The influence of the upstream rough wall also appears in turbulence statistics and instantaneous, coherent structures presented in later sections. The predominant balance below $y^+ \approx 30 - 40$ is between viscous-diffusion and Reynolds-stress terms. Only as the edge of this layer (layer I) is approached, terms that are otherwise zero on a fully developed smooth wall are activated and a new layer develops. Within this new layer (layer II), as noted earlier, the balance is primarily between advective and Reynolds-stress fluxes. This is different from fully developed smooth walls where the balance within the equivalent layer is instead between Reynolds-stress and pressure fluxes, while mean advection is zero. Furthermore, it might be more appropriate to interpret this new layer as two separate regions, IIa and IIb. IIa exists immediately above layer I, and the vertical fluxes due to turbulence stresses point away from wall. The opposite effect occurs in IIb, where turbulence-stress fluxes transport momentum towards the wall. This behaviour of layer IIb is similar to fully developed smooth walls. Within layer II, streamwise turbulence-stress fluxes are already an order of magnitude smaller than their vertical counterparts by $x/\delta = 1$ (not shown in Fig. 6). With downstream distance, the exact point of intersection between IIa and IIb moves away from the wall (see Fig. 6a and b). This is a consequence of the perturbation travelling outwards.

The inner-scaled mean-velocity field for case A is shown in Fig. 7. The abscissa in Fig. 7a does not include the wall displacement height, d , while that in Fig. 7b is normalized using $\delta_{vu} = Re_{\tau u}/\delta$, where $Re_{\tau u}$ is the friction Reynolds number at the upper wall. According to the relations given by Marusic et al. (2013), the logarithmic region (used synonymously with the inertial sublayer) over fully-smooth walls at this Re_{τ} should exist between $90 < y^+ < 140$. Within this wall-normal height, downstream development persists in Fig. 7a. The deficit created by the

roughness decreases with downstream distance, but it prevents a log-law from being established before the end of the computational domain. In terms of mean-momentum budgets, the log-law region is slow to develop primarily due to strong mean-advection effects, which is evident from Fig. 6. Hyperbolic-decline extrapolations of the percentage difference (not shown) between the mean velocity in the developing flow and that at the canonical, smooth-wall level estimates the recovery of the log-law at $x/\delta = 15 - 20$ for the three cases. Here, the log-law is assumed recovered when the aforementioned percentage difference within the specified range of y^+ falls below 2%. Despite its higher k_s^+ , the log-law for the rib-roughened case is the slowest to recover due to a large velocity deficit created after the RTS transition.

At the upper wall, a log-law region identical to the one observed above smooth walls is clearly established in the fully developed regime. This, along with the results of turbulence stresses presented later, point to a virtual insensitivity of this wall to the roughness effects. However, slightly higher u_{τ} (Table 3) and turbulence stress levels (Fig. 8a and b) suggest that the upper wall is not entirely independent of the underlying roughness. After the step change in roughness, \bar{U}^+ at the upper wall shows negligible streamwise development. This statistical picture of the wall layer implies a near-equilibrium velocity field in the transitional regime. The term ‘near’ is chosen because the results discussed in the next section will show that the turbulence field at this wall has not fully attained the canonical state.

5.3. Turbulence statistics

The Reynolds stress profiles are plotted in Fig. 8. The peak of $\overline{u'u'}$ above the rough wall, at $y = 1.09k$, reduces in magnitude while moving away from the lower wall with downstream distance x . A similar trend is shown by $\overline{v'v'}$, $\overline{w'w'}$ and $\overline{u'v'}$ as well. This outward displacement of the

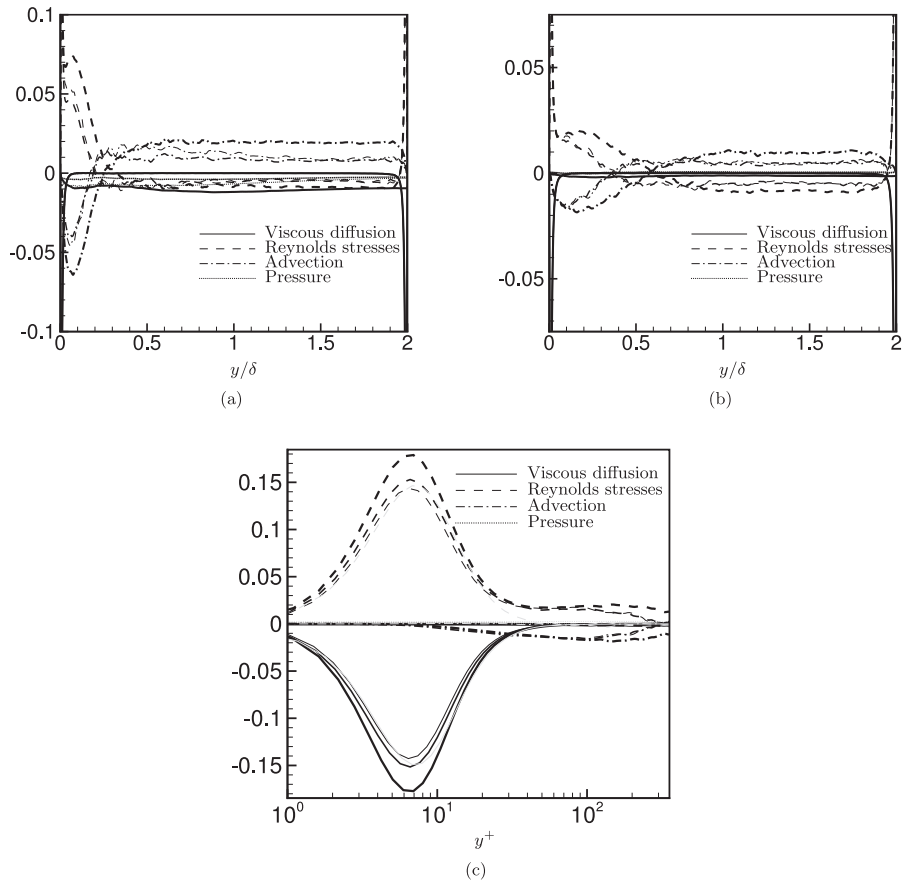


Fig. 6. Mean-momentum budget terms for the three cases in the transitional regime at (a) $x/\delta = 1$, and at (b) $x/\delta = 4$. (c) Near-wall budget terms of the mean momentum in the transitional regime at $x/\delta = 4$. Thinnest lines: case A, thickest lines: case C. Gray lines in (c): fully developed smooth-wall channel. All the terms are on the right hand side of the mean-momentum equation and have been normalized by U_b^2/δ .

peaks can be attributed to the strong, vertical fluxes of mean and turbulence flow fields (Fig. 6). Once their source, the rough wall, is removed, these peaks simply decay while being advected downstream by the mean flow. Tracking this decay with x offers an estimation of the distance needed to approach near fully developed levels. Profiles of the streamwise variation of these outer peaks of $\overline{u'u'}$ are shown in Fig. 8d. Extrapolations of the form,

$$\overline{u'u'}/U_b^2 \text{ lower peaks} \sim e^{\theta(x/\delta)},$$

where θ depends on the roughness size and type, to large x/δ approximate the required distances to first cross the fully-smooth levels at more than 40δ for the cube-roughened cases, and 21δ for the rib-

roughened wall. The peak of $\overline{v'v'}$ above fully developed smooth-walls occurs at $y^+ \approx 100$. This location is the wall-normal height where the log-law region exists in the mean velocity profile (Fig. 7). In the transitional regime, however, the downstream continuations of this turbulence and the mean-flow deficit restricts both the log-law region and the near-wall peak of $\overline{v'v'}$ from becoming established.

In the developing regime, the gross near-wall turbulence structures recover swiftly. Above fully developed smooth-walls, the structures are highly organized, comprising of elongated streamwise coherent motions, that result from strong vertical momentum transport and contribute the bulk of the turbulence kinetic energy (see Kim et al., 1971; Durbin and Reif, 2011; Pope, 2001). The peak of streamwise Reynolds

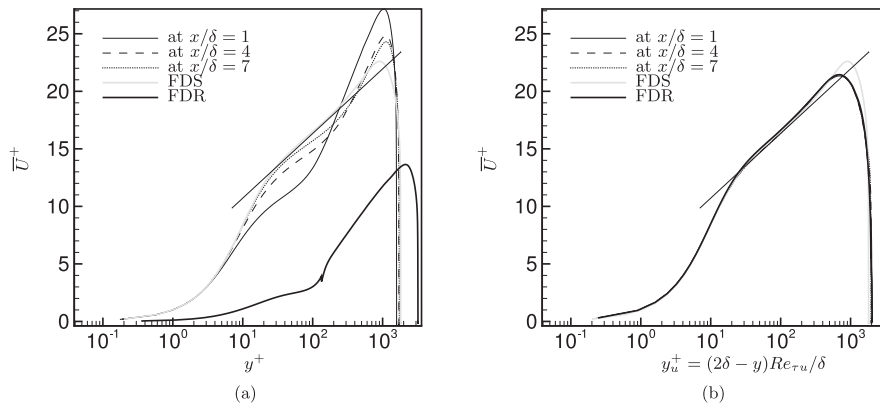


Fig. 7. \overline{U}^+ variation with the streamwise distance for case A. The wall-normal coordinates are in wall units. (a) Scaling from the lower wall, at $y = 0$ and (b) scaling from the upper wall, at $y = 2\delta$. The straight line in both figures is given by: $\overline{U}^+ = (1/0.41)\log(y^+) + 5.1$.

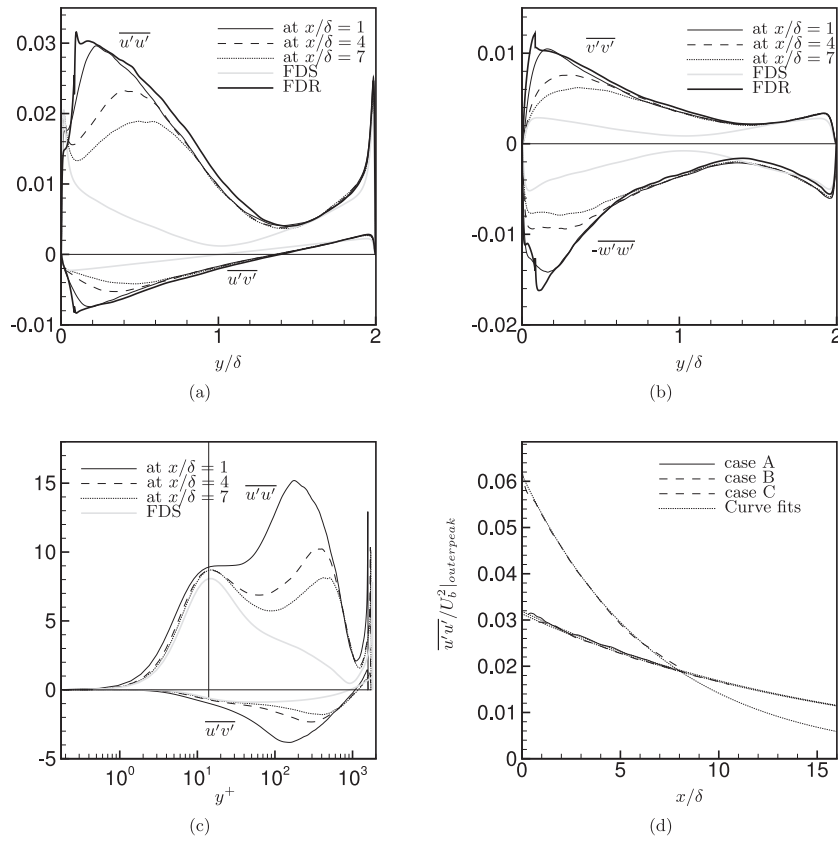


Fig. 8. Reynolds stress terms in the transitional regime for case A, (a) $\overline{u'u'}/U_b^2$ and $\overline{u'v'}/U_b^2$, (b) $\overline{v'v'}/U_b^2$ and $-\overline{w'w'}/U_b^2$, and (c) $\overline{u'u'^+}$ and $\overline{u'v'^+}$. (d) Streamwise (x/δ) variation of the outer peaks of $\overline{u'u'}$.

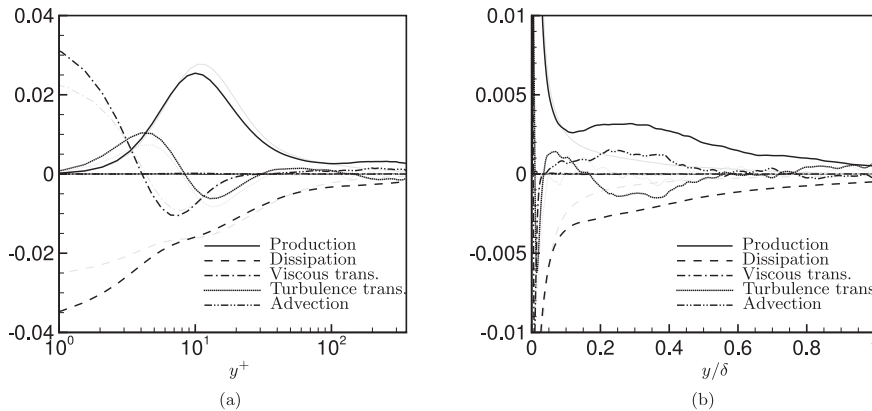


Fig. 9. Budget terms of the turbulence kinetic energy in the transitional regime at $x/\delta = 4$ (a) in the near-wall region and (b) across the lower half of the channel. The pressure-transport term is small near the wall, and therefore not shown. Black lines: case B2; gray lines: fully developed smooth-wall channel. All the terms are on the right hand side of the TKE equation and have been normalized by U_b^2/δ .

stress above such walls is located at $y^+ \approx 14$. By the second streamwise station, at $x/\delta = 4$, this peak has clearly been established, resulting in a double-peaked profile (see Fig. 8c). With downstream distance, it shows negligible wall-normal displacement; its magnitude, however, remains about 8% higher than fully-smooth levels. A similar behaviour is shown by rib-roughened RTS channel flows, case C (also see figure 12d by Ismail et al., 2018). These small differences in magnitudes of $\overline{u'u'}$ exist because although the turbulence structures above fully smooth walls are chiefly re-established, they are still intermittently influenced by large-scale rough-wall structures that have been advected downstream. Further empirical evidence can be established from visualizations of instantaneous motions.

The upper wall remains virtually inactive, displaying little

streamwise change. As evidenced by Fig. 7b, and also clear from Fig. 8, the near-wall turbulence at the upper smooth-wall of the fully-rough regime is nearly identical to that observed above fully-smooth walls. Differences in the magnitudes of turbulence statistics are arguably due to the sporadic interruptions caused by large-scale structures from the lower, rough wall. This nearly smooth-wall profile persists into the transitional regime, where the aforementioned intrusions into the wall layer by large structures of the fluctuating field persist as well.

Compared to the mean-momentum balance presented earlier, the turbulence kinetic energy (TKE) budgets above fully developed smooth walls are slightly more involved and three distinct regions could be defined. The first region occurs very close to the wall, $y^+ \lesssim 40$, and is the most active. Within this region, production (P) exceeds dissipation

(ϵ) in the buffer layer and this excess energy produced is transported towards the wall. The second region, in which $P \approx \epsilon$, is nestled between the first and third regions, and roughly overlaps the logarithmic region. Finally in the third region, the primary balance is between ϵ and turbulence transport, while P is negligible. Like the mean-momentum balance in Fig. 6c, the first region is restored quickly above the developing smooth wall by $x/\delta \approx 2$. Despite this near-complete recovery, ϵ is significantly higher at the wall (Fig. 9a). Additionally, small influences (not shown) of different upstream roughness lengthscales are also present. The other two distinct regions identified above fully developed smooth walls are not reproduced in the transitional regime by the streamwise end of the computational domain. This is evident from Fig. 9b. Also, a balance between P and ϵ is not established, and transport of TKE due to turbulence and advection redistributes energy across the channel. Higher magnitudes of P and ϵ generated by the rough wall merely decay with downstream distance, x , while these transport effects are created as the flow expands after the step change in roughness. The aforementioned enhancement of P above fully developed smooth-wall levels is primarily a consequence of stronger turbulence shear stress rather than mean-velocity gradients.

5.4. Instantaneous motions

Visualizations of instantaneous, turbulent flow fields can offer support to the arguments made earlier regarding the response of flow statistics in the transitional region. Fig. 10 shows contours of the instantaneous, streamwise, fluctuating velocity, u' , in a horizontal plane near the wall from case B. For equivalent fully-smooth flows, this wall-normal location is in the buffer layer at $y^+ \approx 15$. An instantaneous plan view at the same wall-normal height from a separate but complete RTS half-channel simulation with $A_c/A_t = 1/9$ is reported in Fig. 11. This half-channel flow has a wall-normal extent equal to δ , with no-flux boundary conditions applied at the top interface; that makes it like a symmetrically roughened channel.

As early as $x/\delta \approx 1$, elongated streamwise motions are distinguishable in Figs. 10 and 11. These streamwise, alternating coherent structures near the wall are characteristic of fully-smooth turbulent flows (Durbin and Reif, 2011; Pope, 2001). The difference with fully-smooth walls occurs in the form of occasional interruptions by large structures, a few of which are marked by rectangular boxes in Figs. 10 and 11. Contours of xy -planes from case B1 (Fig. 12) suggest the existence of these large structures, of the order δ in size, above the rough

wall. One such large structure over the rough wall is highlighted in Fig. 12. They are comparatively smaller than those above rib-roughened walls, which indicates that their size depends on the roughness size. Additionally, the aforementioned interjections into the wall layers at both walls by these large structures from outer regions of the channel are also evident. Two such interjections are identified in Fig. 12; one at $x/\delta \approx 2.5$ and $y/\delta \approx 0.3$, and another at $x/\delta \approx -2$ and $y/\delta \approx 1.7$. Figs. 10 and 11 are also suggestive of an increase in integral lengthscale of u' from a fully developed rough wall to a developing smooth wall, in both the streamwise and spanwise directions.

Extensive research on smooth-wall turbulent flows has put forward the notion of an autonomous, near-wall ‘cycle’ (e.g. see Jiménez and Moin, 1991; Jimenez and Pinelli, 1999). This ‘cycle’ is chiefly, if not entirely, determined by strong mean shear at the wall. Its wall-normal extent is often defined as the point up to which viscous effects in the mean-momentum budget remain significant. Alternatively, its height can also be thought of as a location above which there is an approximate local equilibrium between production and dissipation of turbulence kinetic energy. Our RTS channel flow results suggest that this near-wall ‘cycle’ is restored almost immediately after the step-change in roughness. This is evidenced by the prompt emergence of near-wall streaks. However, as shown by Figs. 10–12, the cycle is not impervious to the influence of the outer flow and also to the presence of large structures that originate from above the rough wall and persist downstream. This can also be inferred from near-wall, two-point correlations of streamwise velocity in the spanwise direction, R_{uu}^z . Here, R_{uu}^z is calculated as,

$$R_{uu}^z(x) = \frac{\overline{u'(x, z)u'(x, z + \Delta z)}}{\overline{u'u'(x)}}$$

These two-point correlations are plotted in Fig. 13 for case A2 at two heights in the near-wall region. The time averaging for calculating R_{uu}^z is performed for approximately $tU_b/\delta = 25$ time units. Using the location of the first minima from these two-point correlations as the spacing between consecutive high- and low-speed streaks, we can estimate the spacing between two low-speed streaks in a fully developed channel at approximately 100 and 200 wall units in the viscous sublayer and the buffer layer, respectively. This compares favourably with the values reported by Bakewell and Lumley (1967). As noted above while discussing Figs. 10–12, there is a definite enhancement of the spanwise structure size within the transitional regime. This is also indicated by a

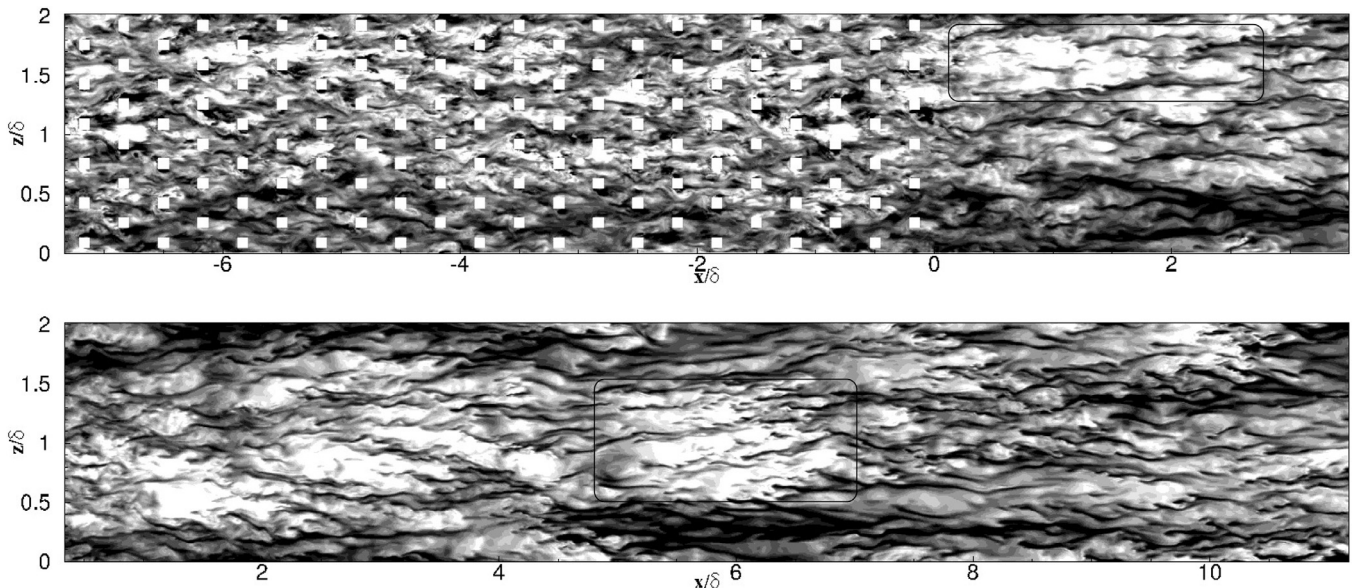


Fig. 10. Instantaneous streamwise velocity fluctuations u' in the xz -plane at $y/\delta = 0.023$ for (a) case B1 and (b) case B2. Scale: white +0.2, black -0.2.

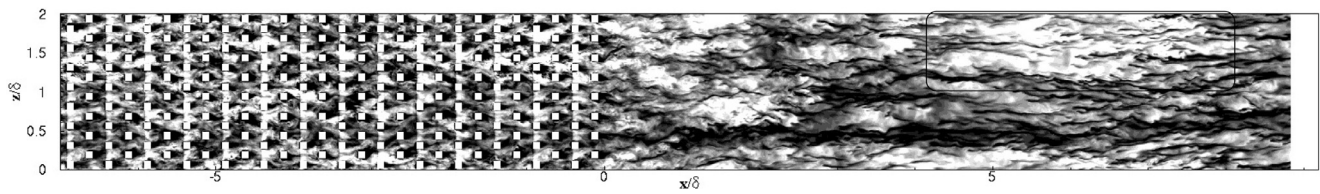


Fig. 11. Instantaneous streamwise velocity fluctuations u' in the xz -plane from a separate cube-roughened, RTS half channel flow simulation at $y/\delta = 0.023$ with $A_c/A_t = 1/9$. Scale: white $+0.2$, black -0.2 .

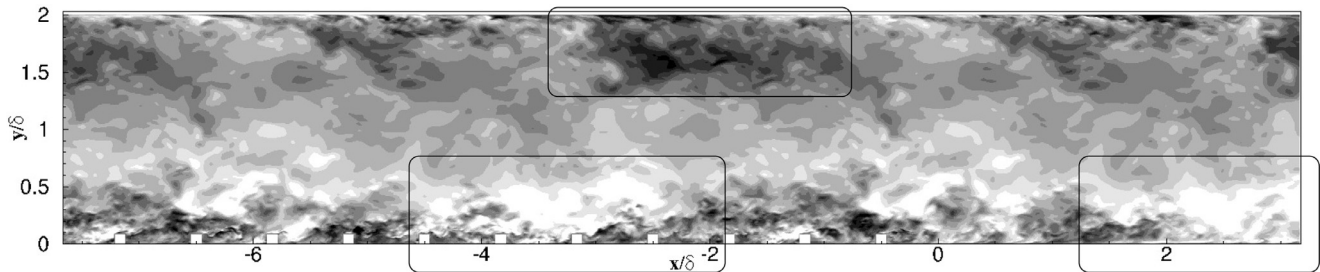


Fig. 12. Instantaneous streamwise velocity fluctuations u' in the xy -plane for case B1 at $z/\delta = 1.25$. Scale: white $+0.25$, black -0.25 .

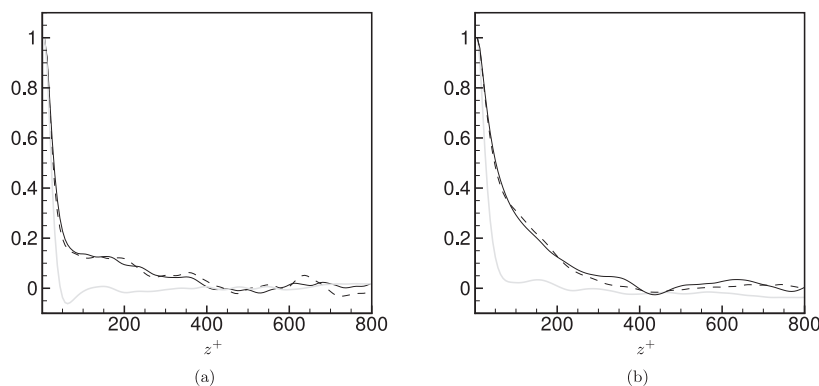


Fig. 13. Two-point correlations, R_{uu}^z , in the spanwise direction at (a) $y^+ = 7$ and (b) $y^+ = 20$ for case A. Solid line: at $x/\delta = 4$, dashed line: at $x/\delta = 7$ and gray line: fully developed smooth-wall channel.

higher value of the integral $\int_0^{L_z} R_{uu}^z dz$ in Fig. 13. Even though the two-point correlations within the transitional regime do not reflect the presence of near-wall streaks, clear evidence of them is available from the surface plots in Figs. 10, 11 and 14 a. Visual inspection of individual streaks from these figures reveals that the spacing among low-speed, elongated motions is of the same order as reported earlier for a fully developed smooth-wall channel.

It is often speculated that the streaks are a consequence of streamwise vortices that displace momentum towards and away from the wall (Blackwelder and Eckelmann, 1979). Fig. 14 examines this effect in the viscous sublayer after the step change in roughness. The elongated streamwise structures are shouldered by strong, streamwise vorticity (one such instance is highlighted by a rectangular box in Fig. 14b); a similar observation is also made above fully developed smooth-wall channels. A high-speed sweeping event can be seen occurring towards the left of the rectangular box in Fig. 14b. Naturally, the conceptual models including the one by Blackwelder and Eckelmann (1979), among others, are not exactly replicated in wall-bounded turbulent flows. Instead, the coherent structures are continuously being contaminated by background, random, non-coherent fluctuations, which is evident from Fig. 14. Finally, the conclusions drawn here also tie up with the discussions in previous sections on near-wall adjustment of the mean-momentum budget (Fig. 6c), the turbulence stresses (Fig. 8c) and the TKE budgets (Fig. 9a).

6. Summary and conclusions

DNS of cube-roughened RTS channel flows are performed, where the fully developed flow over the initial rough-wall regime and the developing flow over the smooth wall have been simulated independently. Cross-flow planes extracted downstream of the rough walls are used as inflow boundary conditions for the developing flow over smooth walls. By the streamwise end of the computational domains, the statistical profiles have not recovered to fully-smooth levels. The skin friction, after an initial strong streamwise variation, plateaus by $x/\delta \approx 1 - 2$, and then shows an exceedingly slow reversion to the fully-smooth magnitudes. For cube-roughened walls, extrapolations to the streamwise variation of the outer peaks of $\overline{u'u'}$ suggest that the distance needed to relax close to fully-smooth levels is of an order 50δ .

Near the lower wall, the relaxation progresses more swiftly, while in the outer flow regions, roughness induced large structures continue to persist throughout the domain. A thin wall layer (below $y^+ \approx 50$), characteristic of fully-smooth walls, re-establishes as early as $x/\delta \approx 1$. This is due to a strong mean shear in close proximity to the wall that occurs after the step change in roughness. Supporting evidence is provided by profiles of mean velocity and turbulence stresses, and by visualizations of instantaneous motions. Above this thin layer, despite the presence of strong shear, a log-law region could not be identified. Arguably, it is the large contribution of mean advection to the momentum balance that prevents a log-law region from being established. This is seen in the mean-momentum budgets (Fig. 6).

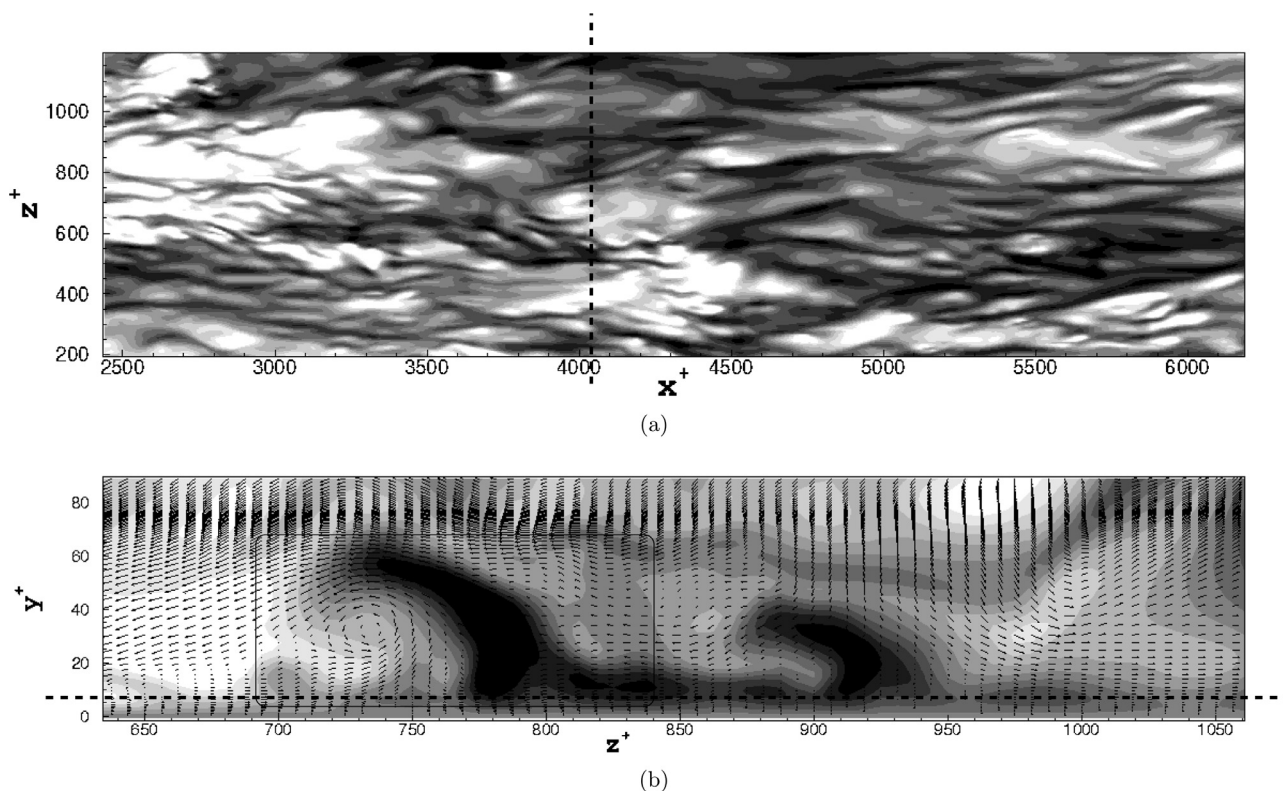


Fig. 14. Instantaneous streamwise velocity fluctuations u' in the (a) xz -plane at $y^+ = 7$ and in the (b) yz -plane at $x/\delta \approx 4.5$ for case A2. The vertical, dashed line in (a) indicates the location of the yz -plane from (b), while the horizontal, dashed line in (b) identifies the location of the xz -plane from (a). The arrows in (b) indicate the two-dimensional vector field: $\vec{G} = W\hat{i} + V\hat{j}$, where unit vectors \hat{i} and \hat{j} represent the horizontal and vertical directions in the figure, respectively. Scale: white $+0.15$, black -0.15 .

The absence of such strong mean shear is responsible for negligible streamwise development at the upper wall. However, the turbulence structure within the fully developed regime at this wall is already in ‘near’ equilibrium.

The observations and conclusions from the present simulations of cube-roughened walls, are generally in congruence with our earlier work on rib-roughened RTS channel flows. The results are, therefore, suggestive of similar flow phenomenology for more general RTS channel flows.

Acknowledgments

This work was supported by the Office of Naval Research under award #N00014-17-1-2200 and by the US Army under contract #W911W6-14-C-0003. Computational resources were provided by NASA’s High-End Computing (HEC) section under award numbers ARMD-15-6415, ARMD-16-7597 and ARMD-18-8100.

References

- Antonia, R.A., Luxton, R.E., 1972. The response of a turbulent boundary layer to a step change in surface roughness. Part 2. Rough-to-smooth. *J. Fluid Mech.* 53, 737–757. <http://dx.doi.org/10.1017/S002211207200045X>.
- Bakewell, H.P., Lumley, J.L., 1967. Viscous sublayer and adjacent wall region in turbulent pipe flow. *Phys. Fluids* 10 (9), 1880–1889. <http://dx.doi.org/10.1063/1.1762382>. <http://aip.scitation.org/doi/abs/10.1063/1.1762382>.
- Blackwelder, R.F., Eckelmann, H., 1979. Streamwise vortices associated with the bursting phenomenon. *J. Fluid Mech.* 94 (3), 577–594. <http://dx.doi.org/10.1017/S0022112079001191>.
- Durbin, P.A., Reif, B.A.P., 2011. *Statistical Theory and Modeling for Turbulent Flows*. Wiley.
- Falgout, R.D., Yang, U.M., 2002. *hypre: A Library of High Performance Preconditioners*. Springer Berlin Heidelberg, Berlin, Heidelberg, pp. 632–641.
- Frenzen, P., Vogel, C.A., 1995. On the magnitude and apparent range of variation of the von Karman constant in the atmospheric surface layer. *Boundary Layer Meteorol.* 72

(4), 371–392.

- Hanson, R.E., Ganapathisubramani, B., 2016. Development of turbulent boundary layers past a step change in wall roughness. *J. Fluid Mech.* 795, 494–523. <http://dx.doi.org/10.1017/jfm.2016.213>.
- Ikeda, T., Durbin, P.A., 2002. *Direct Simulations of a Rough-Wall Channel Flow*. Stanford University, Flow Physics and Computation Division, Dept. of Mechanical Engineering Report No. TF-81.
- Ikeda, T., Durbin, P.A., 2007. Direct simulations of a rough-wall channel flow. *J. Fluid Mech.* 571, 235–263. <http://dx.doi.org/10.1017/S002211200600334X>.
- Ismail, U., Zaki, T.A., Durbin, P.A., 2018. Simulations of rib-roughened rough-to-smooth turbulent channel flows. *J. Fluid Mech.* 843, 419–449. <http://dx.doi.org/10.1017/jfm.2018.119>.
- Ismail, U., Zaki, T.A., Durbin, P.A., 2017. Turbulence statistics in rib-roughened rough-to-smooth (RTS) channel flows. Tenth International Symposium on Turbulence and Shear Flow Phenomena (TSFP10), Chicago, IL, USA, July 2017. http://tsfp10.org/TSFP_program/2/316.pdf.
- Jackson, P.S., 1981. On the displacement height in the logarithmic velocity profile. *J. Fluid Mech.* 111, 15–25. <http://dx.doi.org/10.1017/S0022112081002279>.
- Jiménez, J., Moin, P., 1991. The minimal flow unit in near-wall turbulence. *J. Fluid Mech.* 225, 213–240.
- Jimenez, J., Pinelli, A., 1999. The autonomous cycle of near-wall turbulence. *J. Fluid Mech.* 389, 335–359. <http://dx.doi.org/10.1017/S0022112099005066>.
- Kim, H., Kline, S.J., Reynolds, W.C., 1971. The production of turbulence near a smooth wall in a turbulent boundary layer. *J. Fluid Mech.* 50 (1), 133–160.
- Leonardi, S., Castro, I.P., 2010. Channel flow over large cube roughness: a direct numerical simulation study. *J. Fluid Mech.* 651, 519–539. <http://dx.doi.org/10.1017/S002211200999423X>.
- Leonardi, S., Orlandi, P., Smalley, R.J., Djenidi, L., Antonia, R.A., 2003. Direct numerical simulations of turbulent channel flow with transverse square bars on one wall. *J. Fluid Mech.* 491, 229–238.
- Marusic, I., Monty, J.P., Hultmark, M., Smits, A.J., 2013. On the logarithmic region in wall turbulence. *J. Fluid Mech.* 716.
- Moser, R.D., Kim, J., Mansour, N.N., 1999. Direct numerical simulation of turbulent channel flow up to $Re_\tau = 590$. *Phys. Fluids* 11 (4), 943–945. <http://dx.doi.org/10.1063/1.869966>.
- Nikuradse, J., 1933. *Laws of flow in rough pipes* (in German). VDI-Forsch. 361 (translation in NACA Tech. Rep. 1292 (1950). National Advisory Commission for Aeronautics).
- Orlandi, P., Leonardi, S., Antonia, R.A., 2006. Turbulent channel flow with either transverse or longitudinal roughness elements on one wall. *J. Fluid Mech.* 561, 279–305.
- Pierce, C.D., Moin, P., 2004. Progress-variable approach for large-eddy simulation of non-

- premixed turbulent combustion. *J. Fluid Mech.* 504, 73–97. <http://dx.doi.org/10.1017/S0022112004008213>.
- Pope, S.B., 2001. *Turbulent flows*.
- Raupach, M.R., Antonia, R.A., Rajagopalan, S., 1991. Rough-wall turbulent boundary layers. *Appl. Mech. Rev* 44 (1), 1–25.
- Renard, N., Deck, S., 2016. A theoretical decomposition of mean skin friction generation into physical phenomena across the boundary layer. *J. Fluid Mech.* 790, 339–367.
- Squire, D.T., Morrill-Winter, C., Hutchins, N., Schultz, M.P., Klewicki, J.C., Marusic, I., 2016. Comparison of turbulent boundary layers over smooth and rough surfaces up to high reynolds numbers. *J. Fluid Mech.* 795, 210–240.